Original

Purkiani, K.; Becherer, J.; Floeser, G.; Graewe, U.; Mohrholz, V.;
Schuttelaars, H.M.; Burchard, H.:

Numerical analysis of stratification and destratification processes in a tidally energetic inlet with an ebb tidal delta

Journal of Geophysical Research : Oceans (2015) AGU

DOI: 10.1002/2014JC010325

AGU PUBLICATIONS

JGR

Journal of Geophysical Research: Oceans

RESEARCH ARTICLE

10.1002/2014JC010325

Key Points:
- Within a tidal inlet, dynamics at two nearby stations is different
- A baroclinic numerical 3-D model is able to reproduce these differences
- Weak lateral stratification is enhanced due to narrowing of the channel

Correspondence to:
H. Burchard,
hans.burchard@io-warnemuende.de

Citation:
Purkiani, K., J. Becherer, G. Flöser, U. Gräwe, V. Mohrholz, H. M. Schuttelaars, and H. Burchard (2015), Numerical analysis of stratification and destratification processes in a tidally energetic inlet with an ebb tidal delta, *J. Geophys. Res. Oceans, 120*, 225–243, doi:10.1002/2014JC010325.

Received 23 JUL 2014
Accepted 16 DEC 2014
Accepted article online 23 DEC 2014
Published online 21 JAN 2015

Numerical analysis of stratification and destratification processes in a tidally energetic inlet with an ebb tidal delta

Kaveh Purkiani[1], Johannes Becherer[1], Götz Flöser[2], Ulf Gräwe[1], Volker Mohrholz[1], Henk M. Schuttelaars[3], and Hans Burchard[1]

[1]Leibniz Institute for Baltic Sea Research Warnemünde, Warnemünde, Germany, [2]Helmholtz-Zentrum Geesthacht, Institute for Coastal Research, Geesthacht, Germany, [3]Delft Institute of Applied Mathematics, Delft University of Technology, Delft, Netherlands

Abstract Stratification and destratification processes in a tidally energetic, weakly stratified inlet in the Wadden Sea (south eastern North Sea) are investigated in this modeling study. Observations of current velocity and vertical density structure show strain-induced periodic stratification for the southern shoal of the tidal channel. In contrast to this, in the nearby central region of the channel, increased stratification is already observed directly after full flood. To investigate the processes leading to this different behavior, a nested model system using GETM is set up and successfully validated against field data. The simulated density development along a cross section that includes both stations shows that cross-channel stratification is strongly increasing during flood, such that available potential energy is released in the deeper part of the channel during flood. An analysis of the potential energy anomaly budget confirms that the early onset of vertical stratification during flood at the deeper station is mainly controlled by the stratifying cross-channel straining of the density field. In contrast to this, in the shallow part of the channel, the relatively weak cross-channel straining is balanced by along-channel straining and vertical mixing. An idealized analytical model confirms the following hypothesis: The laterally convergent flood current advecting laterally stratified water masses from the shallow and wide ebb tidal delta to the deep and narrow tidal channel has the tendency to substantially increase cross-channel density gradients in the tidal channel. This process leads to stratification during flood.

1. Introduction

In tidal estuaries, the major along-channel processes of vertical stratification due to horizontal density gradients are closely related to generation mechanisms of estuarine circulation, such as gravitational circulation [*Pritchard*, 1952, 1954; *Hansen and Rattray*, 1965] and tidal straining [*Simpson et al.*, 1990; *Jay and Musiak*, 1994]. If the tidal energy is high enough to completely destratify the water column at a certain phase of the tide, SIPS (strain-induced periodic stratification) [*Simpson et al.*, 1990] occurs. For estuaries with only small cross-channel variation, this occurs typically at the end of flood. Using a one-dimensional water column model, *Burchard and Hetland* [2010] showed that for tidally energetic estuaries with SIPS occurrence, tidal straining is the major mechanism generating estuarine circulation and thus stratification. A suitable measure for the competition between the stratifying process of tidal straining and the destratifying process of turbulent mixing is the Simpson number

$$\mathrm{Si}=\frac{\langle\overline{\partial_x b}\rangle\langle H\rangle^2}{U_*^2}, \tag{1}$$

with the depth-averaged tidal mean horizontal buoyancy gradient $\langle\overline{\partial_x b}\rangle$, the tidal mean water depth $\langle H\rangle$, and the root mean square bed friction velocity scale U_*. Note that the buoyancy $b=-(g/\rho_0)(\rho-\rho_0)$ is a scaled density with potential density ρ, reference density ρ_0, and gravitational acceleration g. In estuaries with relatively small cross-channel variation, SIPS may occur for low Si numbers in the range of $0.1 \leq \mathrm{Si} \leq 0.6$ [see, e.g., *Burchard et al.*, 2013]. Permanent stratification would be expected for $\mathrm{Si} > 1$ [*Monismith et al.*, 1996]. Estuarine convergence due to narrowing or widening of tidal channels may complicate this picture by increasing or decreasing estuarine circulation and thus stratification [*Ianniello*, 1979; *Burchard et al.*, 2014].

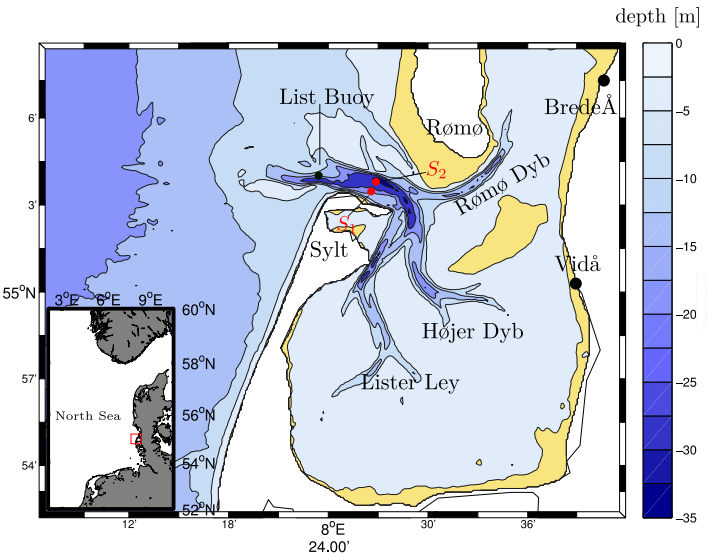

Figure 1. Map of the study site, with the eastern North Sea (inserted map) and details of the Sylt-Rømø Bight (large map). The bathymetry values are color coded, with areas above mean sea level marked in yellow. The two discrete freshwater sources are marked as black dots, and the field stations S_1 and S_2 are marked as red dots. The location of the List buoy is indicated as a black dot.

Nunes and Simpson [1985] realized that cross-channel bathymetric variation may play a major role in estuarine physics, simply because differential advection between the deep tidal channel with high flow velocity and the shoals with reduced flow velocity leads to cross-channel density gradients that force cross-channel exchange currents. The fundamental impact of cross-channel dynamics on estuarine circulation was systematically investigated by *Lerczak and Geyer* [2004] and by *Burchard et al.* [2011] using idealized numerical models and by *Huijts et al.* [2009] using an analytical model. All studies show that the impact of cross-channel circulation on estuarine circulation and stratification can be significant. *Burchard and Schuttelaars* [2012] showed that cross-channel circulation directly results in enhanced along-channel tidal straining circulation, a residual circulation component driven by tidal straining as defined by *Burchard and Hetland* [2010]. Numerical studies of the Hudson River estuary [*Scully et al.*, 2009; *Scully and Geyer*, 2012] support the assumption of strong cross-channel influences on estuarine stratification and circulation. These authors explained the increased stratification during flood by a balance between along-channel advection, cross-channel advection, and tidal asymmetries in turbulent mixing. For a tidally energetic inlet with laterally located freshwater discharge inside the embayment, *Buijsman and Ridderinkhof* [2008] find significant generation of two-cell secondary circulation which during flood is driven by salinity with higher values in the channel center as compared to the channel sides [see also *Nunes and Simpson*, 1985; *Lerczak and Geyer*, 2004]. In contrast to that, the lateral freshwater sources drive an internal pressure gradient during ebb which results in a one-cell secondary circulation. Coriolis acceleration is assumed to be small but partially supporting the secondary circulation. *Lacy et al.* [2003] reports observations in a tidal channel in San Francisco Bay showing increasing cross-channel density gradients during flood tide with significant impacts on stratification and turbulent mixing.

The role of residual circulation in tidal estuaries in sediment transport has been documented in a number of modeling [*Festa and Hansen*, 1978; *Geyer*, 1993; *Burchard and Baumert*, 1998; *Chernetsky et al.*, 2010] and field studies [e.g., *Lang et al.*, 1989; *Jay and Musiak*, 1994; *Sanford et al.*, 2001]: at the landward end of the salt intrusion, sediment is accumulating and results in the occurrence of an estuarine turbidity maximum.

In the Wadden Sea, the dynamics is different from macrotidal estuaries, with the horizontal density gradients being generated both by sources of freshwater (small rivers and groundwater) and differential heating and precipitation [*Burchard et al.*, 2008] such that nonzero density gradients extend to the ends of the tidal embayments. It has been postulated by *Burchard et al.* [2008] that these density gradients drive a sediment pumping mechanism into the Wadden Sea which might explain parts of the observed sediment import [*Postma*, 1961]. Long-term observations of water velocity profiles and salinity in the North German Wadden Sea confirm this hypothesis [*Flöser et al.*, 2011]. *Beusekom and de Jonge* [2002] additionally highlighted the importance of particulate organic matter import for nutrient cycling in the Wadden Sea.

During a field campaign in a tidally energetic inlet in the Wadden Sea, it was observed that the stratification at the southern shoal of the channel (location S_1; see Figure 1) is controlled by classical along-channel tidal straining, as shown by *Becherer et al.* [2011], with a stratifying tendency during ebb and a destratifying tendency during flood. In contrast to that, significant stratification at the nearby station S_2 in the center of the

channel is occurring directly after full flood, a phenomenon which could not be explained by *Becherer et al.* [2011]. These contrasting observations motivate our numerical model study which we designed to analyze how in this tidal inlet the composition of stratification and destratification processes can vary significantly over such short distances. The environmental significance of the water column stability is given by its impact on residual circulation and transport of solutes and particulate matter.

In the present paper, we used a process-resolving (100 m $\times$ 100 m horizontal resolution) three-dimensional coastal ocean model to reproduce the observations that were collected during 15–17 April 2008 in the Sylt-Rømø Bight (see Figure 1). Observations, model setup, and the method of analyzing the potential energy anomaly are presented in section 2. The contrasting observations at both sites in the tidal inlet are presented and discussed in section 3 and used for model validation in section 4. The model data are then analyzed in section 5 to identify the relevant stratifying and destratifying processes, and in section 6, we explain the sudden onset of flood stratification by an analytical model. Finally, some conclusions are drawn in section 7.

2. Material and Methods

2.1. Site Description

The study area of the Sylt-Rømø Bight is located in the northern Wadden Sea between the islands of Sylt and Rømø, situated in the southeastern part of the North Sea. The water is exchanged through the Lister Dyb, a 2.5 km wide and up to 40 m deep tidal inlet connecting the back-barrier area of the islands with the North Sea (Figure 1). On the seaward side of the deep channel, an ebb tidal delta with typical depths of 5–10 m is present. The entire area of the Sylt-Rømø Bight is about 410 km^2 including 190 km^2 of intertidal flats. The total basin freshwater input includes two small rivers (Brede Å and Vidå, see the black dots in Figure 1) with seasonally varying discharges between 4 and 10 $m^3\ s^{-1}$ and an annual rainfall of 0.8 m. The tide is semidiurnal with an average tidal range of about 1.8 m and a significant diurnal inequality due to diurnal tidal components. The tidal prism which is defined as the water volume difference between mean high water and mean low water is about 4.8×10^8 m^3. The tidal catchment is drained through the three tidal channels Rømø Dyb, Højer Dyb, and Lister Ley (see Figure 1). The intersection of these three bended channels results in a complicated topography at the main inlet of the Sylt-Rømø Bight, the Lister Dyb. Both the Sylt and Rømø islands are connected to the mainland by artificial dams. As a consequence of these constructions, the Sylt-Rømø Bight is semienclosed and thus an ideal natural laboratory for studying water circulation and sediment transport. A number of observational studies [*Andersen et al.*, 2000; *Andersen and Pejrup*, 2001; *Becherer et al.*, 2011] and modeling studies [*Lumborg and Windelin*, 2003; *Lumborg and Pejrup*, 2005; *Burchard et al.*, 2008] have been carried out in this region.

2.2. Numerical Model Description

For the model simulation in this study, the General Estuarine Transport Model (GETM, www.getm.eu) [*Burchard and Bolding*, 2002; *Burchard et al.*, 2004] is applied. GETM is a three-dimensional baroclinic open source model with hydrostatic and Boussinesq assumptions, especially developed for applications in shallow coastal regions with substantial drying and flooding of intertidal flats. In this model, the three-dimensional hydrostatic momentum equations are solved on a staggered C-grid, which is horizontally Cartesian in the present application. To calculate vertical turbulent transports, GETM uses turbulence closure models from the General Ocean Turbulence Model (GOTM, www.gotm.net) [*Umlauf and Burchard*, 2005], and in the present study, a k-ε model is used with an algebraic second moment closure. In order to vertically discretize the model equations, the water column is resolved with 25 equidistant σ-layers. Higher-order positive-definite advection schemes are used for the advective momentum, temperature, and salinity transports as well as for the advective transports of the turbulent quantities k (turbulent kinetic energy) and ε (dissipation of k into heat). High-resolution coastal ocean simulations using GETM including drying and flooding of intertidal flats have been carried out before by *Stanev et al.* [2003], *Burchard et al.* [2004], *Banas et al.* [2007], *Burchard et al.* [2008], and *Duran-Matute et al.* [2014].

Due to the complex, small-scale bathymetry of the Lister Dyb, where data from the two nearby field stations showed substantially different dynamics, a high spatial resolution of at least 100 m is required. The gridded bathymetry is shown in Figure 2 for the southern part of the Lister Dyb in comparison to data from high-resolution multibeam soundings. It can be seen that the major larger-scale bathymetric features are

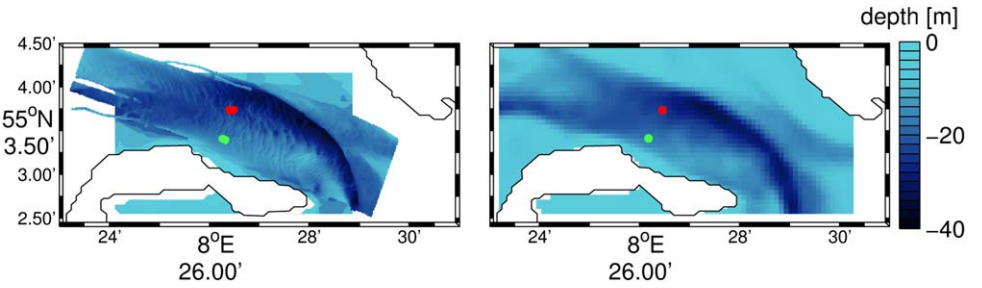

Figure 2. (left) Observed and (right) gridded bathymetry in the southern part of the Lister Dyb. Exact locations of stations S_1 (green dot) and S_2 (red dot) are indicated. Note that in the left figure the accurate positions are given for each observed hydrographic profile.

resolved, but many differences are obvious on the smaller scales. To improve the comparison between observed and simulated profiles, the locations for the extraction of station data from model results have been shifted slightly within a small search radius of $\leq$ 200 m relative to the exact (but due to ship movement temporally varying) locations of the observed profiles (see Figure 2). In order to reproduce larger-scale effects such as the tidal wave propagating along the Wadden Sea coast or the coast-to-sea density gradient, a one-way nesting approach is followed here. The large-scale model for the German Bight has a resolution of 1800 m and is laterally forced by surface elevation, temperature, and salinity obtained from the operational model of the German Maritime and Hydrographic Agency (BSH). An intermediate resolution (600 m) model for the northern Wadden Sea and the finest resolution model for the Sylt-Rømø Bight (100 m) are nested into these coarser models. Meteorological forcing is provided for all three model domains from the operational model of the German Weather Service Local Model (DWD-LM) with a horizontal resolution of 7 km. These data include wind velocity and direction at 10 m above the sea surface, air temperature, and dew point temperature at 2 m above sea level, air pressure, precipitation, and total cloud cover every 3 h. The comparison of simulated wind velocity and observed local data during the campaign shows good agreement. Air-sea fluxes of momentum, heat, and freshwater are calculated inside GETM by using the bulk formulae based on *Kondo* [1975]. The daily river discharge is specified as the freshwater input at four different locations for the Elbe and Weser rivers (large model domain) and the Brede Å and Vidå rivers (small model domain). Since the medium-scale (coarse-resolution) northern Wadden Sea model does not properly resolve the salinity and temperature gradients inside the Sylt-Rømø Bight, the initial conditions for the high-resolution model are corrected within the embayment in such a way that average horizontal temperature and salinity gradients result in a horizontal buoyancy gradient of $\partial_x b = 10^{-6}$ s^{-2}, a value which is roughly in agreement with the observations by *Becherer et al*. [2011]. Without this correction, the time to dynamically generate the observed horizontal buoyancy gradient would take too long. To bring these initial conditions into dynamical balance with the external forcing, the model simulation is initialized on 1 October 2007, and then continued until 30 April 2008 to cover the observational period. In the high-resolution model, the barotropic time step is set to 2.5 s, whereas the baroclinic mode is integrated every 60 s. The model setup is divided into 70 subdomains which are distributed on a computer cluster with 12 processors for parallel computation.

2.3. Potential Energy Anomaly

As a tool for quantifying stratification and destratification processes in coastal regions, *Simpson and Bowers* [1981] introduced the potential energy anomaly (PEA) as the amount of mechanical energy (per m^3) required to homogenize the entire water column with a given density stratification:

$$\phi = \frac{1}{D}\int_{-H}^{\eta} gz(\bar{\rho}-\rho)\mathrm{d}z, \tag{2}$$

where z is the vertical coordinate from the bottom at $z=-H$ to the sea surface at $z=\eta$, and $D=\eta+H$ is the water depth, ρ is the density profile, and $\bar{\rho}$ is the depth-mean density. Based on this definition, $\phi=0$ is obtained for a fully mixed water column, positive values indicate stable stratification and negative values represent unstable stratification. Based on the budget equations for temperature and salinity, *Burchard and Hofmeister* [2008] analytically derived a budget equation for the PEA, of which the terms most relevant for the present study are:

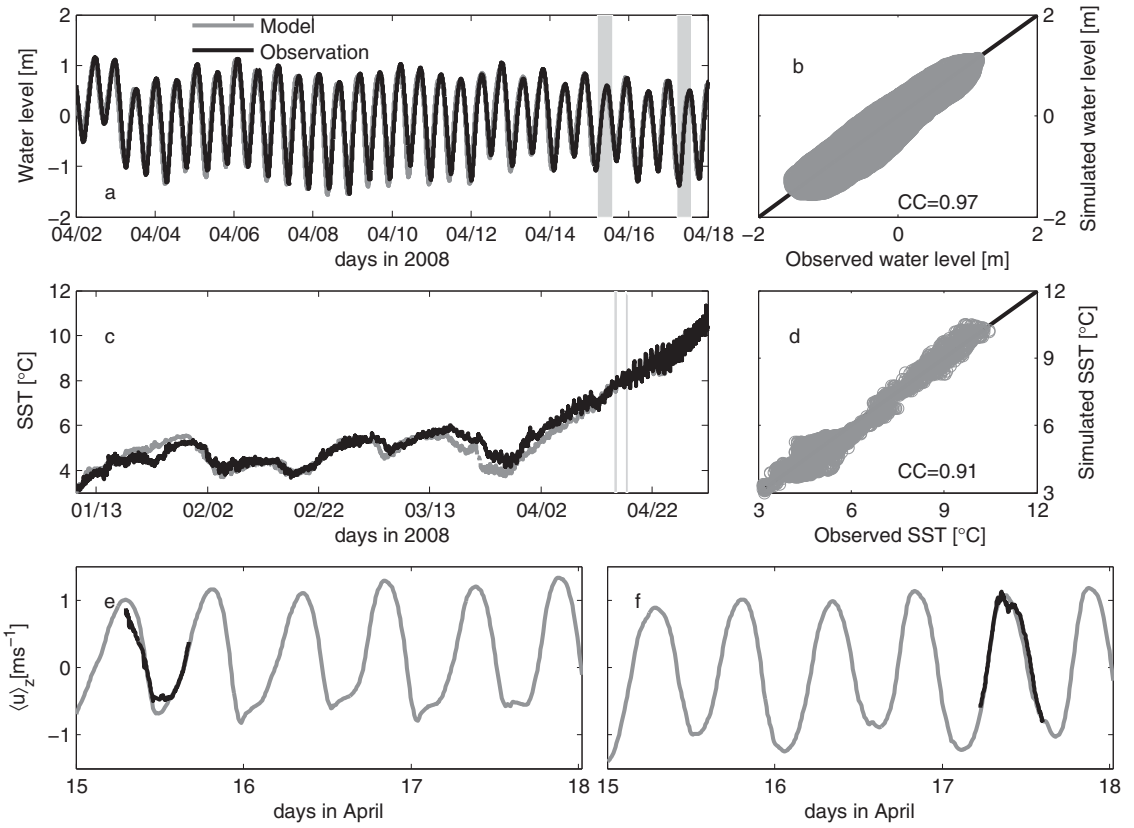

Figure 3. Long-term validation of model simulations against observations: (a) simulated (gray) versus observed (black) sea surface elevation at the tidal gauge in List/Sylt during 2–19 April 2008; the two campaign periods are indicated as gray bars; (b) scatterplot of simulated versus observed sea surface elevation in List/Sylt during the period shown in Figure 3a; (c) simulated (gray) versus observed (black) sea surface temperature (SST) in List/Sylt; the two campaign periods are indicated as gray lines; (d) scatterplot of the SST data during the period shown in Figure 3c; (e) simulated (gray) versus observed (black) depth-mean along-channel velocity at S_1 during the campaign; (f) same as Figure 3e, but for S_2. In Figures 3b and 3d, the correlation coefficient (CC) between observations and model results is given.

$$\partial_t\phi = \underbrace{-\nabla_h\cdot(\overline{\boldsymbol{u}}\phi)}_{\text{A}} \underbrace{+\frac{g}{D}\nabla_h\bar{\rho}\cdot\int_{-H}^{\eta}z\tilde{\boldsymbol{u}}\,\mathrm{d}z}_{\text{B}} \underbrace{-\frac{g}{D}\int_{-H}^{\eta}\left(\eta-\frac{D}{2}-z\right)\tilde{\boldsymbol{u}}\cdot\nabla_h\tilde{\rho}\,\mathrm{d}z}_{\text{C}} \underbrace{-\frac{g}{D}\int_{-H}^{\eta}\left(\eta-\frac{D}{2}-z\right)\tilde{w}\partial_z\tilde{\rho}\,\mathrm{d}z}_{\text{D}} \underbrace{+\frac{\rho_0}{D}\int_{-H}^{\eta}P_b\,\mathrm{d}z}_{\text{E}}+\ldots, \tag{3}$$

where an overbar indicates depth-mean values and a tilde indicates deviation from the depth-mean value, with the buoyancy production P_b, the horizontal velocity vector $\boldsymbol{u}$, and the vertical velocity component w. In equation (3), the first term indicated by A is horizontal advection of ϕ (**Advx** and **Advy**), B is the depth-mean straining (**Sx** and **Sy**, i.e., the change in stratification due to straining of the depth-mean horizontal density gradient $\nabla_h\bar{\rho}$ by the sheared exchange flow $\tilde{u}$). Note that bold abbreviations denote terms in Figures 12 and 13. C quantifies changes in ϕ due to straining resulting from deviations from the depth-mean density gradient (nonmean straining, **nSx** and **nSy**, i.e., the correlation between horizontal currents and horizontal density gradients), D drives changes in ϕ due to vertical advection, and E drives changes in ϕ due to the vertical mixing of density (**Mix**, causing reduction of ϕ during stable stratification). Terms for inner sources or sinks of ϕ or effects of horizontal mixing are omitted (see *Burchard and Hofmeister* [2008] for further details). Note that *De Boer et al*. [2008] derived a comparable budget equation for ϕ.

3. Field Observations

Observations in the Lister Dyb tidal inlet were carried out during 15–17 April 2008. On 15 and 17 April, measurements were taken from an anchored research vessel at stations S_1 and S_2 (Figure 1), with water

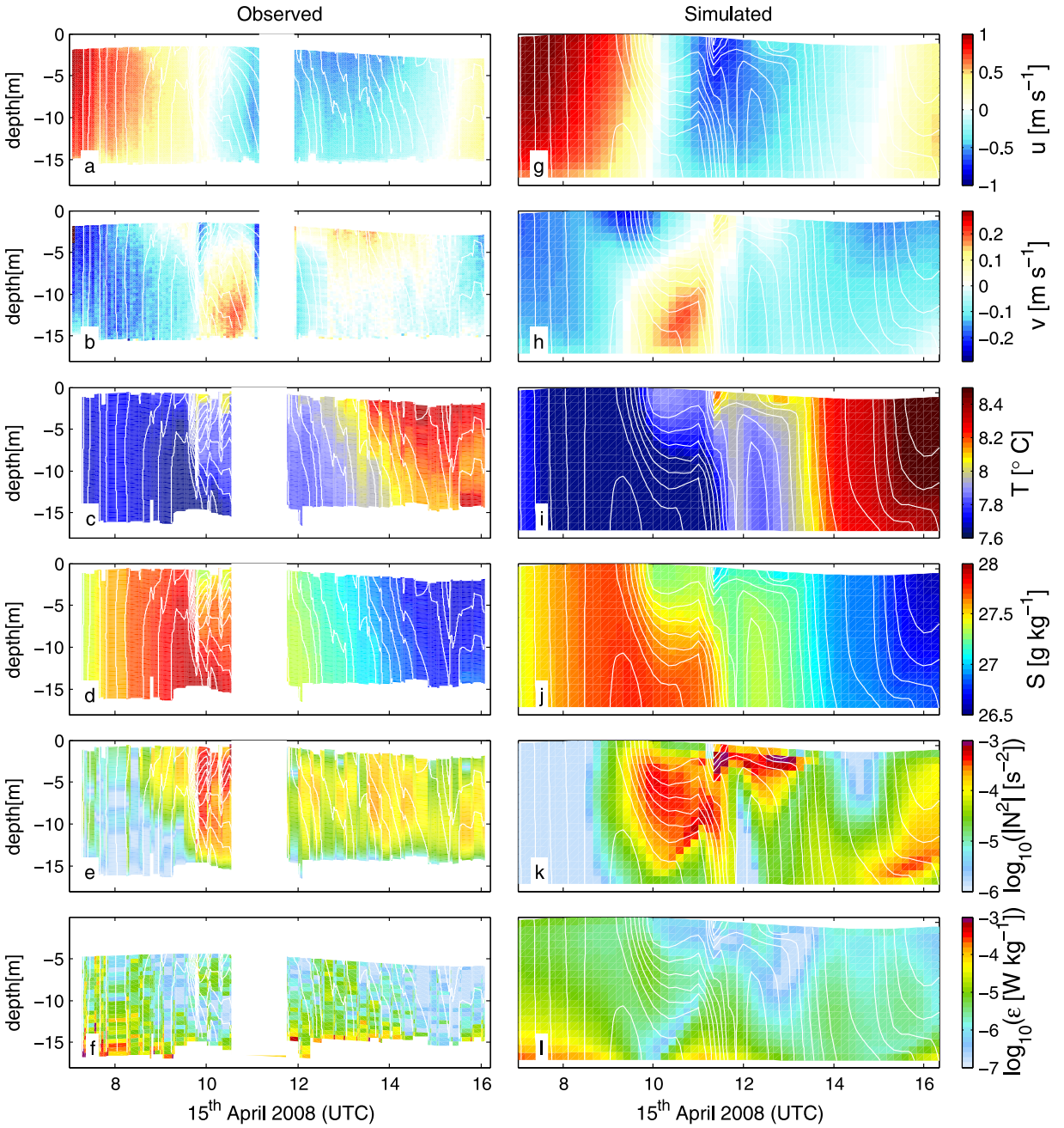

Figure 4. (left) Observed and (right) simulated vertical profiles on 15 April 2008 at station S_1 (shallow channel). (a and g) Along-channel current velocity; (b and h) cross-channel current velocity; (c and i) potential temperature; (d and j) salinity; (e and k) buoyancy-frequency; and (f and l) dissipation rate. The white lines in each plot show isopycnals. Areas with missing values are blanked.

depth of 14.8 and 23.2 m, respectively. The current velocity was measured by a vessel-mounted Acoustic Doppler Current Profiler (ADCP), and data were averaged over 180 s to reduce noise. A multiprobe Conductivity-Temperature-Depth (CTD) profiler was used to measure conductivity, temperature, pressure, fluorescence, and optical backscatter. Furthermore, several turbulent parameters were measured by a free-falling MSS90 microstructure profiler. Hydrographically, the typical spring situation was present, with salinity being lower and temperature being higher in the Wadden Sea than further offshore, leading to a positive buoyancy gradient into the Wadden Sea (see the climatology data by *Burchard et al.* [2008]). During the observations in mid-April 2008, neap tide was present, with a tidal elevation amplitude of about 1 m and a clear diurnal inequality due to the presence of diurnal tides amounting to an amplitude of about 0.2 m (Figure 3). A harmonic analysis of tidal gauge data from List harbor (not shown here in detail) identifies

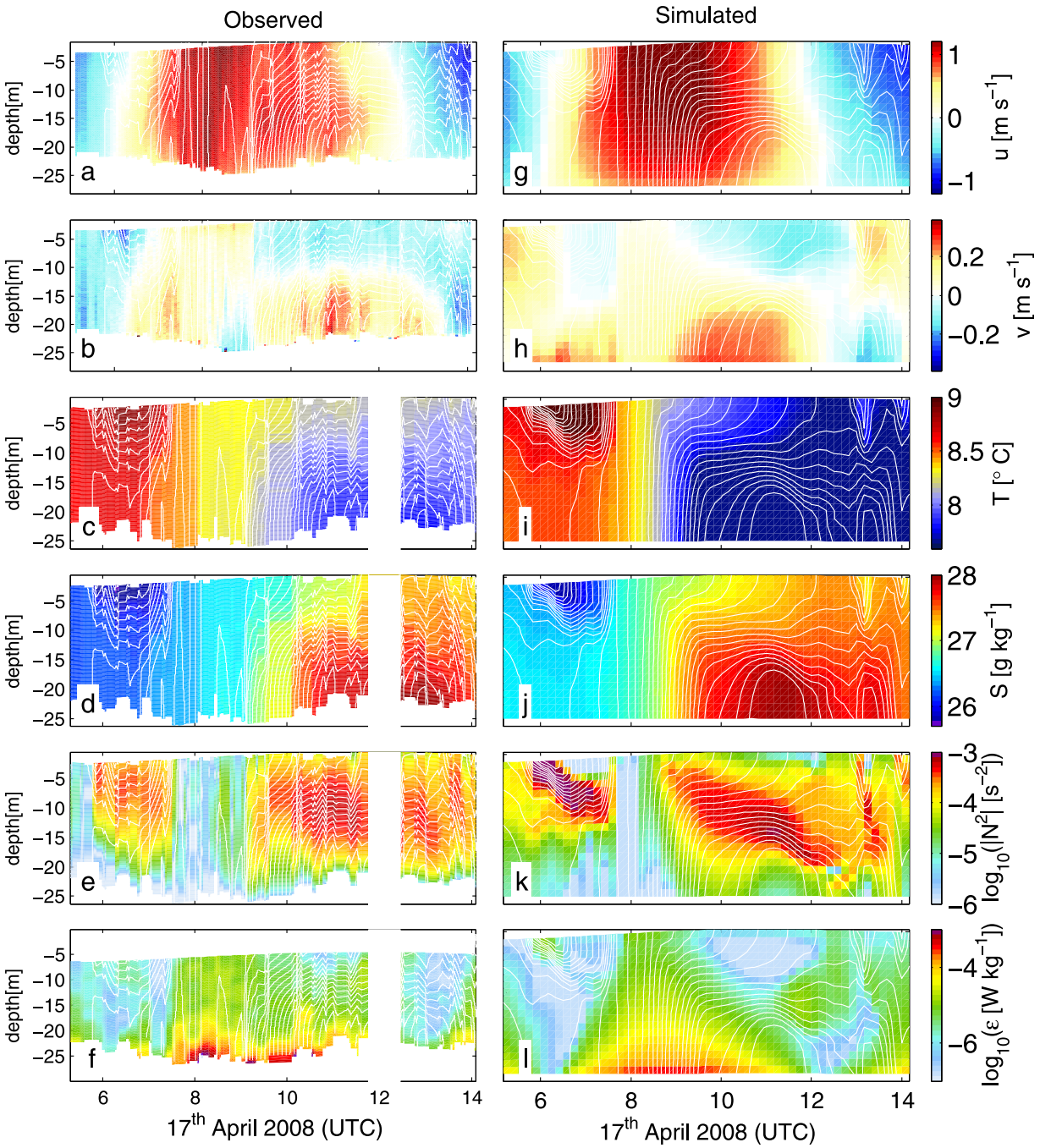

Figure 5. (left) Observed and (right) simulated vertical profiles on 17 April 2008 at station S_2 (deep channel). (a and g) Along-channel current velocity; (b and h) cross-channel current velocity; (c and i) potential temperature; (d and j) salinity; (e and k) buoyancy-frequency; and (f and l) dissipation rate. The white lines in each plot show isopycnals. Areas with missing values are blanked.

significant values of the diurnal O_1 (0.1 m) and K_1 (0.07 m) tidal amplitudes. Wind was relatively weak and thus with negligible dynamic effects during the campaign. For more details, see *Becherer et al.* [2011].

The station observations are shown in Figures 4 and 5, left. The data in S_1, as already presented by *Becherer et al.* [2011], reflect the tidal straining situation as discussed by *Simpson et al.* [1990] (see also the data by *Rippeth et al.* [2001]). The water column is destratified during flood (positive current velocity), when salinity increases and temperature decreases. It becomes significantly stratified during the slack after flood ($N^2 \approx 10^{-3}$ s^{-2}) and remains marginally stratified ($N^2 \approx 10^{-4}$ s^{-2}) during the subsequent ebb phase (Figures 4a–4e). The dissipation rate is therefore slightly higher during flood than during ebb (Figure 4f).

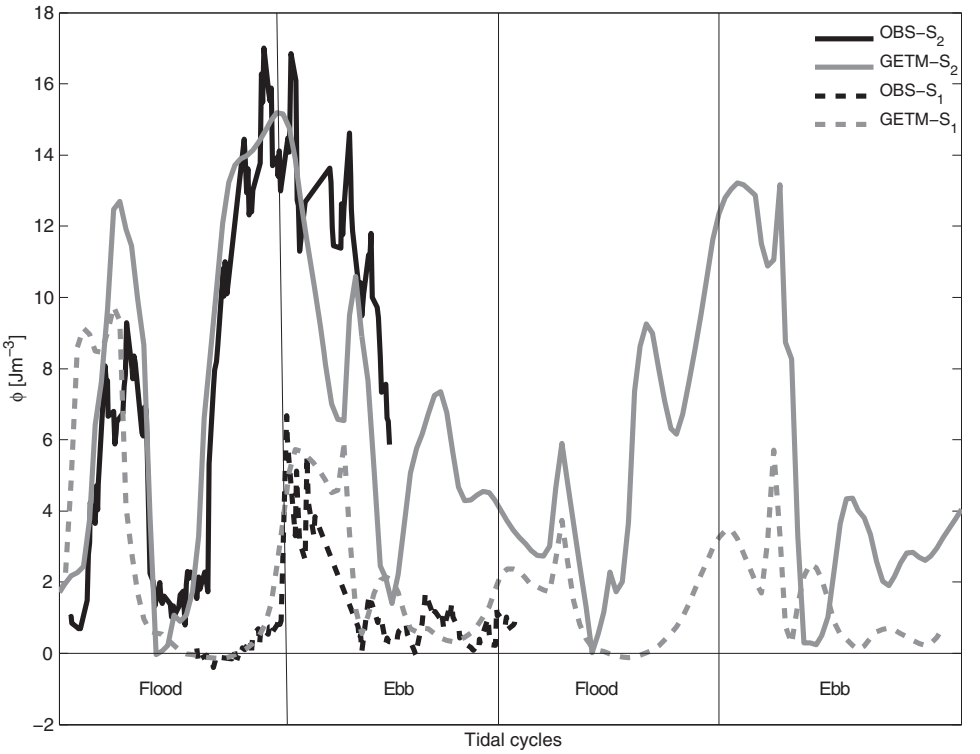

Figure 6. Potential energy anomaly (PEA), during 15 and 17 April with time relative to high water. Dotted and full black lines indicate the observed PEA in station S_1 (15 April) and S_2 (17 April), and the dotted and full gray lines show simulated PEA at the same positions and times.

Although stratification seems to be explained here by only the longitudinal dynamics [*Becherer et al*., 2011], lateral circulation seems to play a role at S_1 (Figure 4b). At slack after flood and into the early ebb, a cross-channel exchange current with up to 0.15 m s^{-1} is generated, indicating that buoyancy is increasing toward the center of the channel. In Figure 6 the stability of the water column is shown using the PEA time series at S_1 (dotted black line): it is around zero during flood, indicating a well-mixed water column, it has a distinct peak during slack after flood, and has marginally positive values during ebb. It should be noted that the significant stratification after flood may already be an indication of a deviation from the classical situation. At least the observations by *Rippeth et al*. [2001] of a situation without lateral stratification and also the simulations of these data by *Simpson et al*. [2002] do not indicate stratification during slack after flood. It must therefore be assumed that lateral stratification plays a role in the Lister Dyb.

The profile data at station S_2 are presented in the left plots of Figure 5. At slack after ebb (6:00–7:00 h), strong salinity and temperature stratification develops over the entire water column see (Figures 5c and 5d), leading to peak values of $N^2 \approx 10^{-3}s^{-2}$ (Figure 5e). Tidal turbulence has almost ceased as seen in the low dissipation rate data (Figure 5f). At the onset of the flood (7:00–8:00 h), salinity and temperature stratification gets eroded from the bottom upward, as turbulence increases. At full flood (8:00–9:00 h), velocity, salinity, and temperature profiles are almost vertically homogeneous through the entire water column, allowing increased values of dissipation rate higher up into the water column. Until this moment, the situation is comparable to classical SIPS. But as flood progresses (9:00–12:00 h), temperature and salinity profiles become vertically stratified, a situation which lasts until the end of the observations at early ebb (14:00 h). Together with this sudden onset of stratification, a strong cross-channel exchange flow develops at the end of full flood (Figure 5b), directed toward the north near the bottom, with a bottom to surface velocity difference of about 0.3 m s^{-1}, again indicating increasing buoyancy toward the north. It may already here be speculated that this exchange current is generating the sudden flood stratification. This unexpected behavior is also reflected in the development of the PEA at station S_2 (Figure 6) which already increases directly after full flood, after it has been eroded during the first 2 h of flood. This has already been shown by *Becherer et al*. [2011], who also used a number of single CTD profiles taken on 16 April along a transect to show

that there is a smooth spatial transition from the more classical situation at S_1 to the more complex behavior at S_2.

4. Model Validation and Results

In order to validate the model results, long-term data of sea surface elevation and sea surface temperature (SST) obtained from a monitoring buoy located within the Lister Dyb tidal channel (see Figure 1 for the position of the buoy) are used. Furthermore, campaign data for profiles of current velocity, temperature, salinity, buoyancy frequency, and dissipation rate are compared to model results to assess the quality of the model simulations during this period.

4.1. Long-Term Model Validation

The validation of the sea surface elevation in Figures 3a and 3b shows that model results closely follow the observations with a correlation coefficient (CC) of 0.97, resulting in a root mean square error (rmse) of 0.067 m between data and model result.

Also for the SST, the quantitative agreement between observational data and model results is excellent, with a CC of 0.91 and an rmse of 0.68 K. Long-term salinity and velocity time series are not available, such that we refer to the short-term validation data available for the campaign periods (see next section).

4.2. Process-Based Model Validation

The model results for the PEA (Figure 6) show that for both stations, the dynamics of stratification and destratification is well reproduced by the model: at S_1, stratification is slightly unstable during the last phase of flood, whereas at S_2 stratification strongly increases directly after full flood. At S_1, the maximum PEA is less than half of the PEA at S_2, probably mainly due to the deeper water at S_2 which leads to an increased Simpson number which, in turn, is indicative for stronger stratification.

Details of the simulated development of profiles of current velocity, temperature, salinity, buoyancy frequency, and dissipation rate are shown in Figures 4 and 5 of which the observations have already been discussed in section 3.

For station S_1, the phase and amplitude of the along-channel and cross-channel current velocity is well reproduced (Figures 4g and 4h). Also, for temperature and salinity, the agreement between model simulation and observations is acceptable (Figures 4i and 4j), although the observed profiles are more continuously stratified than the simulated profiles which show a distinct pycnocline at middepth. At slack after flood temperature and salinity become strongly stratified, as seen in the observations, but the model stratifies about half an hour too late. During ebb, temperature increases and salinity decreases again, although in a less gradual way than observed. It looks as if after full ebb, a water mass with slightly decreased temperature and increased salinity passes by, a feature which is not present in the observations at S_1. This simulated feature which is not occurring in the model simulations at other tidal periods has a weak impact on the PEA only, because the pycnocline is simply pushed further up (and intensified) toward the surface by this different water mass. Since the overall dynamics of the inlet are seemingly not influenced by this singular event which may have been generated by an eddy having branched off far upstream, we are not further considering this deviation between model and observations. In contrast to the observations, simulated stratification is more surface intensified during the first phase of ebb and more bottom intensified during the second phase of ebb, as seen in the values for N^2 (Figure 4k), but the overall stratification is comparable as seen in the PEA values (Figure 6). As for the simulated dissipation rate (Figure 4l), some gross agreement with the (relatively noisy) observations is seen with highest values at flood, minimum values during slack after flood and increased level during ebb.

At the deep station S_2, the agreement between model simulations and observations (Figure 5) is even better than at the nearshore and shallower station S_1. Observed current velocity profiles are well reproduced with the flood currents lasting slightly longer at middepth than at the surface (Figure 5g), a process which is indicative for the presence of estuarine circulation. The significant lateral exchange flow setting on after full flood is clearly present in the model simulations (Figure 5h). Both simulated temperature and salinity are becoming strongly stratified already during full flood, as in the observations (Figures 5i and 5j). The buoyancy frequency shows that also here the simulated stratification (Figure 5k) is biased toward the upper half

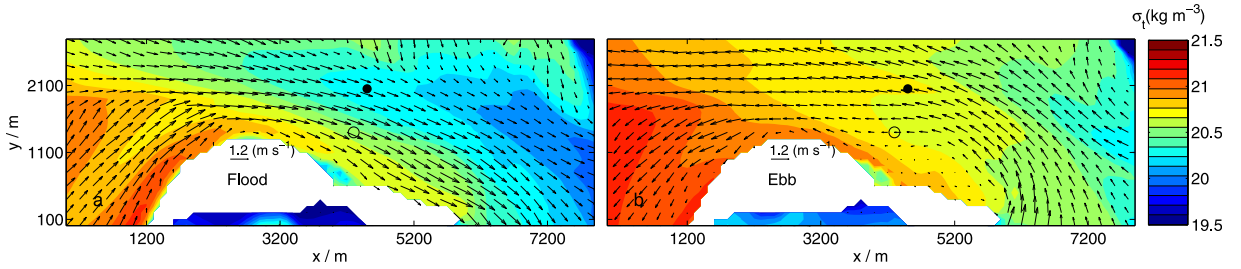

Figure 7. Surface velocity (arrows) and surface density anomaly σ_t (contours) in the southern part of the Lister Dyb (left) averaged over a flood tide and (right) averaged over an ebb tide on 17 April 2008. Station S_1 is marked by an open circle, and station S_2 is marked by a filled circle.

of the water column, although this effect is much weaker than at S_1. The gross features of the observed dissipation rate (Figure 5l) are again reproduced by the model simulations.

The differences between model simulations and observations are most likely due to unresolved or underresolved topographical features (see section 2.2 and Figure 2) and chaotic eddying motion which in general make model-data comparisons of vertical profiles a difficult task. We do however conclude that the quantitative agreement is sufficient for a model-based analysis of stratifying and destratifying processes.

5. Analysis of Model Results

In this section, model results are analyzed to explain the different behavior of the cycle of stratification and destratification between the two stations S_1 and S_2. To obtain a consistent and synoptic comparison of the dynamics between stations S_1 and S_2, the flood-ebb cycle during 17 April (for parts of which observational data are available for station S_2) is mainly considered here.

5.1. Density Dynamics

To give an estimate for the local forcing conditions of tidal straining, Figure 7 shows for flood and ebb surface velocity and surface density anomaly for a region around the two stations S_1 and S_2. Conditions are shown for 17 April 2008 for which observations are not available at station S_1, but the situation is comparable on 15 April (not shown). Highly variable along-channel and cross-channel density gradients are visible such that complex tidal straining patterns are expected.

Density distribution during a tidal cycle is shown in Figure 8 for the reference transect through the stations S_1 and S_2. At the onset of the flood, a weakly stratified water column is present across the entire transect, remaining from low turbulent mixing during slack after ebb (Figure 8a). As the flood progresses, the entire transect becomes vertically homogenized due to strong vertical mixing, with water in the thalweg showing lower densities than at the slopes of the channel (Figure 8b). Then, after full flood, the density on the southern shoal (left in the figure) has substantially increased the cross-channel density gradient with the consequence that cross-channel circulation (Figure 8g) which was already visible at full flood triggers strong stratification in the center of the channel during late flood (Figure 8c). While station S_1 at the southern shoal remains well mixed, station S_2 becomes strongly stratified, which is consistent with the observations shown in Figures 4 and 5. An inspection of Figure 7a shows that there seems to be an efficient pathway for dense water northward along the western shore of Sylt and around the northernmost point of the island toward the southern part of the Lister Dyb. Figure 9 gives evidence for this efficient pathway for dense water along the northern coast of Sylt. The residual currents along almost the entire coast are flood directed, due to the curvature of the coast, which leads to two residual eddies, one west and one east of the northernmost point of Sylt. The residual along-coast current is thus flood dominated and transports water along the coast which is denser than the water in the center of the tidal channel. The positive along-channel buoyancy gradient (equivalent to negative density gradient) seen in Figure 9 reflects the classical density gradient for a spring situation and the positive (increased buoyancy toward the channel center in the north) across-channel gradient is partially driven by the residual flood-directed current along the coast, and partially due to the fact that the major riverine freshwater supply is located in the northern part of the Sylt-Rømø Bight [*Burchard et al.*, 2008].

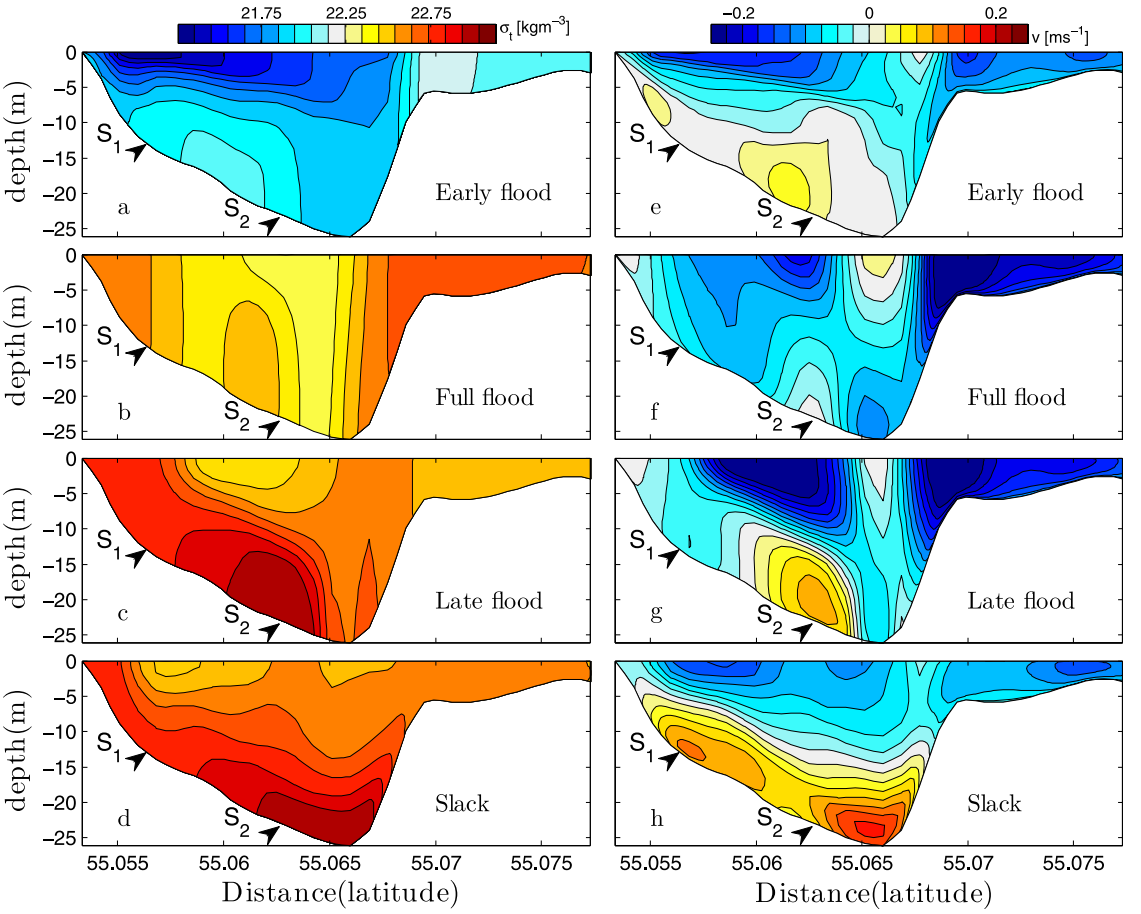

Figure 8. Density and lateral velocity across a reference transect through stations S_1 and S_2 during a flood tidal cycle on 17 April 2008. The left arrow marks station S_1, and the right arrow marks station S_2.

The overall patterns in Figure 8 look similar to Figure 4 by *Lacy et al.* [2003] showing density across a tidal channel in San Francisco Bay. Also, there during the flood, salinity is highest at the southern shoal (with flood currents coming from the west) and salinities and their cross-channel gradients increasing in time, leading to enhanced stratification. There, the higher salinities at the southern shoal are due to the flood currents entering from the south-west. Also, similar between our study site and the channel in San Francisco Bay studied by *Lacy et al.* [2003] is the fact that the channel widens and shallows toward the west.

Further inspection of Figure 8d shows that at slack after flood the entire channel is filled with stratified water, which is slowly eroded during ebb flow. Lateral density gradients are low during ebb, probably due to relatively homogeneous water masses being advected from the Wadden Sea. However, during ebb some marginal stability of the water column remains, as already shown for the profile observations and model data (Figures 4 and 5).

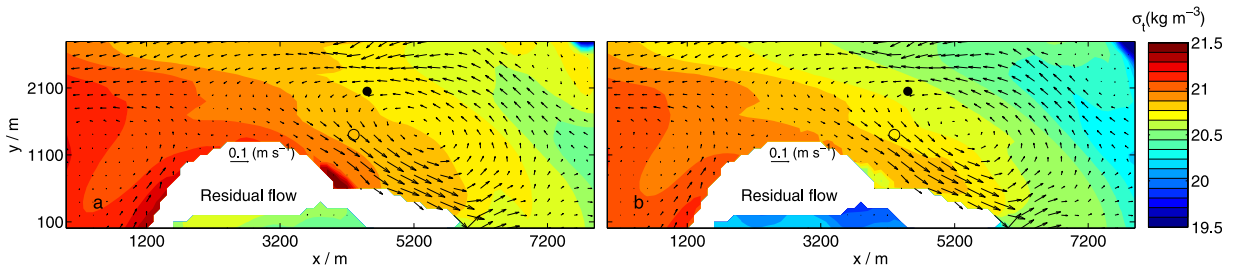

Figure 9. Tidally averaged depth-mean current (arrows) and density (contours) in the southern part of the Lister Dyb (left) on 15 April 2008 and (right) on 17 April 2008. Station S_1 is marked by an open circle, and station S_2 is marked by a filled circle.

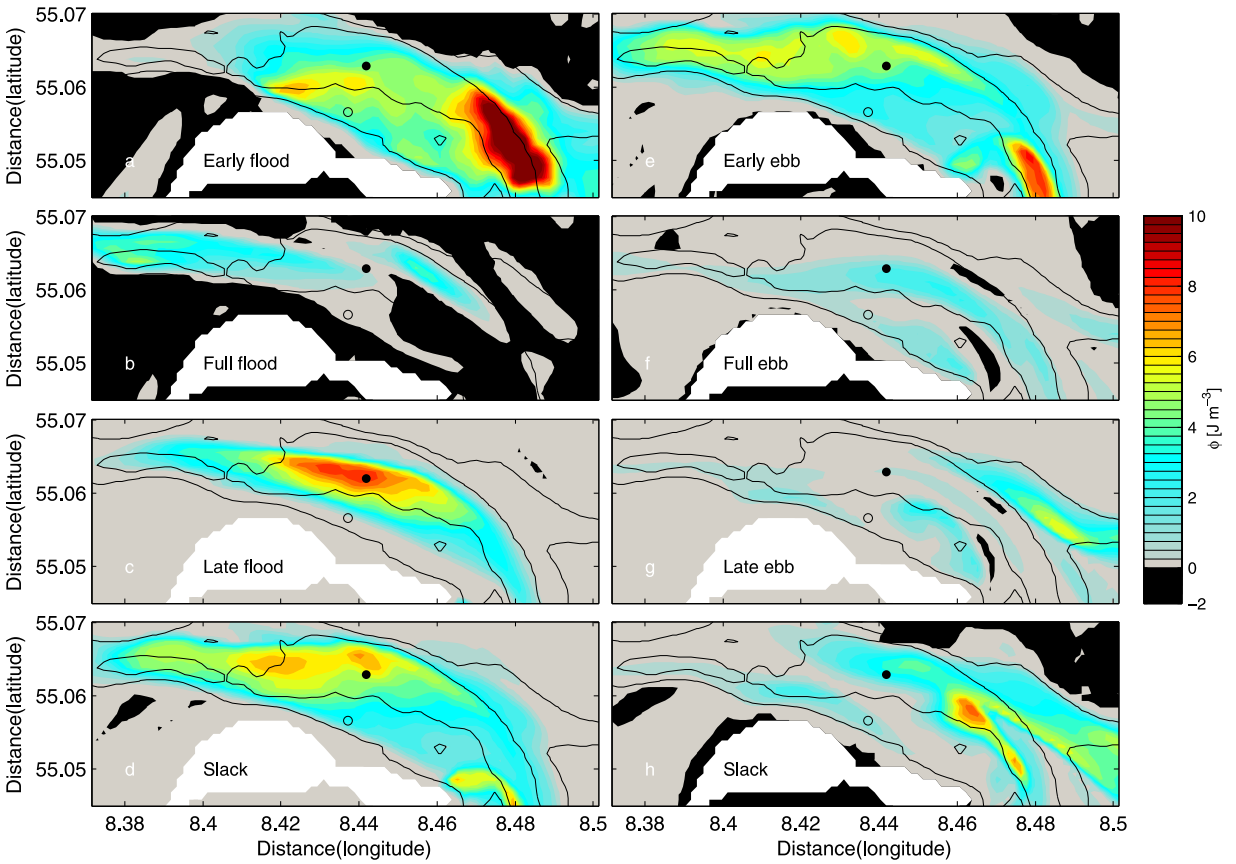

Figure 10. Spatial and temporal dynamics of the potential energy anomaly ϕ during different parts of the tidal cycle in the Lister Dyb. Station S_1 is marked by an open circle, and station S_2 is marked by a filled circle. The black lines show the 10 and 20 m isobaths.

5.2. PEA Dynamics

At early flood, the entire deep part of the channel shows relatively strong stratification with values typically larger than 10 J m^{-3} (Figure 10a). During the course of the flood tide, the stratification is reduced due to the impact of mixing such that values are below 3 J m^{-3} with unstable stratification in large areas (Figure 10b), although cross-channel density gradients are already high in this phase of the tide (Figure 8). During late flood, due to the release of the built up available potential energy, stratification increases again, mainly in the center of the deep part of the channel, where station S_2 is situated, with values larger than 8 J m^{-3} (Figure 10c). These values are significantly larger than the values at S_2 during early flood, as already seen in Figure 6. In contrast to that, stratification at S_1 was stronger during early flood than during late flood, a result for which observations were not available. The stratification built up during late flood is further increased during slack after flood, and then eroded again during ebb, however a marginal stability was still observed.

To quantitatively investigate which process is leading to the late flood stratification in the center of the tidal channel, depth-mean along-channel and cross-channel straining terms (term B in (3)) for the potential energy anomaly are calculated and displayed in Figure 11 for full flood and full ebb. The discrimination between the two components is made such that the along-channel straining **Sx** is defined as the straining along the tidally averaged depth-mean velocity. The cross-channel straining **Sy** is then orthogonal to the latter. As a result, during flood the generally positive (stratifying) cross-channel straining term is dominant over the generally negative (destratifying) along-channel straining term. Together with the negative mixing term, along-channel straining is not strong enough in the deep part of the channel (station S_2) to dominate over the stratifying effect of cross-channel straining. In contrast to that, at station S_1, destratifying along-channel straining and mixing are about balancing stratifying cross-channel straining such that a significant stratification cannot develop.

During ebb, along-channel straining is largely positive (as expected), but cross-channel straining has a more complex structure along the bathymetric slopes showing both signs. Interestingly, just at S_1, the along-channel straining is slightly negative, but marginal stratification is still built up due to lateral straining.

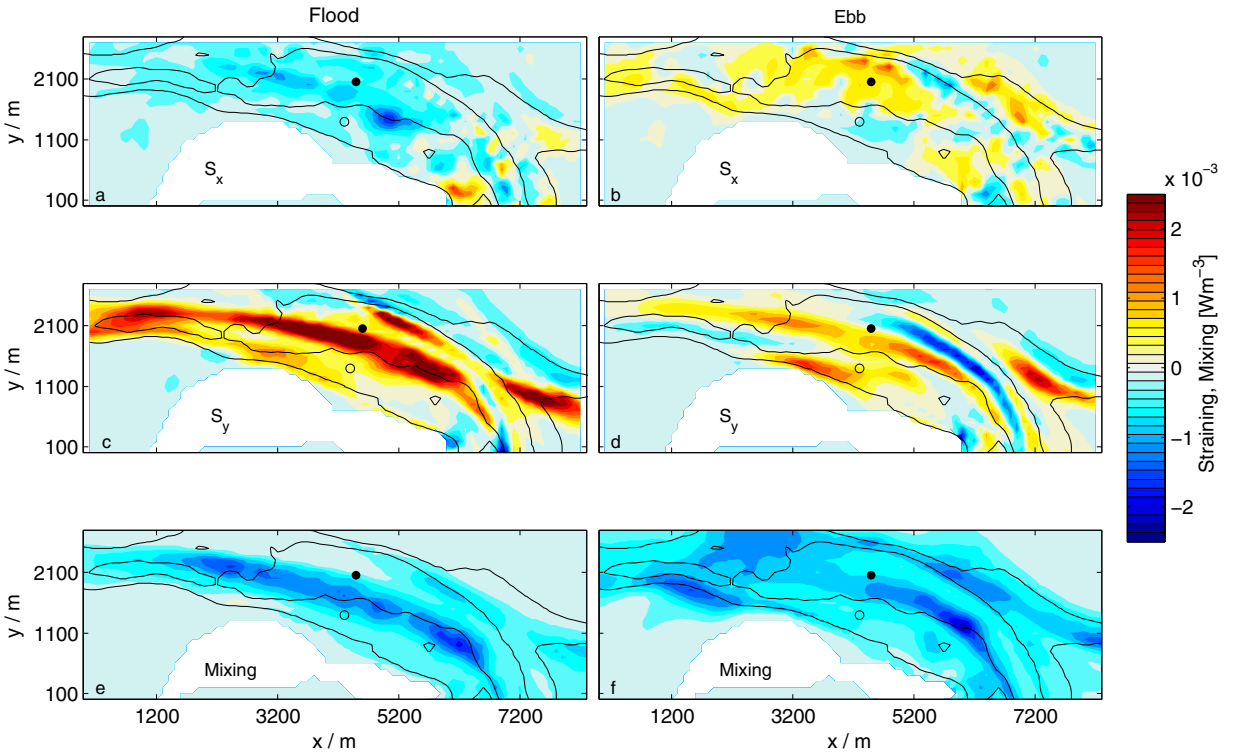

Figure 11. Simulated along-channel (**Sx**) and cross-channel (**Sy**) depth-mean straining, and mixing during flood and during ebb in the southern part of Lister Dyb on 17 April 2008. The black lines show the 10 and 20 m isobaths.

In Figures 12 and 13, time series of the major forcing terms for the potential energy anomaly equation (3) are calculated to quantitatively understand the difference between the two stations. For both stations, the sum of all calculated forcing terms is compared to the temporal change of ϕ to check numerical consistency

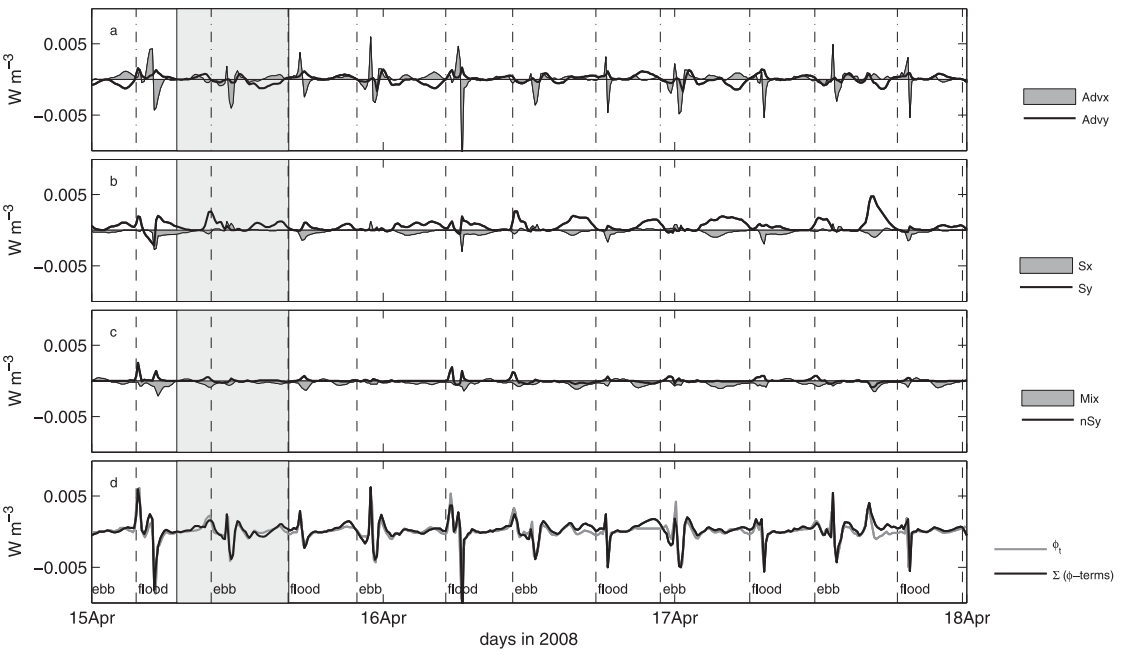

Figure 12. Balance for potential energy anomaly according to equation (3) at station S_1. (a) Along-channel and across-channel advection, **Advx** and **Advy**; (b) along-channel and across-channel straining, **Sx** and **Sy**; (c) vertical mixing, **Mix**, and nonmean across-channel straining, **nSy**; (d) comparison between tendency term and right-hand side of (3), ϕ_t and $\Sigma(\phi$-terms). The gray-shaded area shows the observational period on 15 April at station S_1.

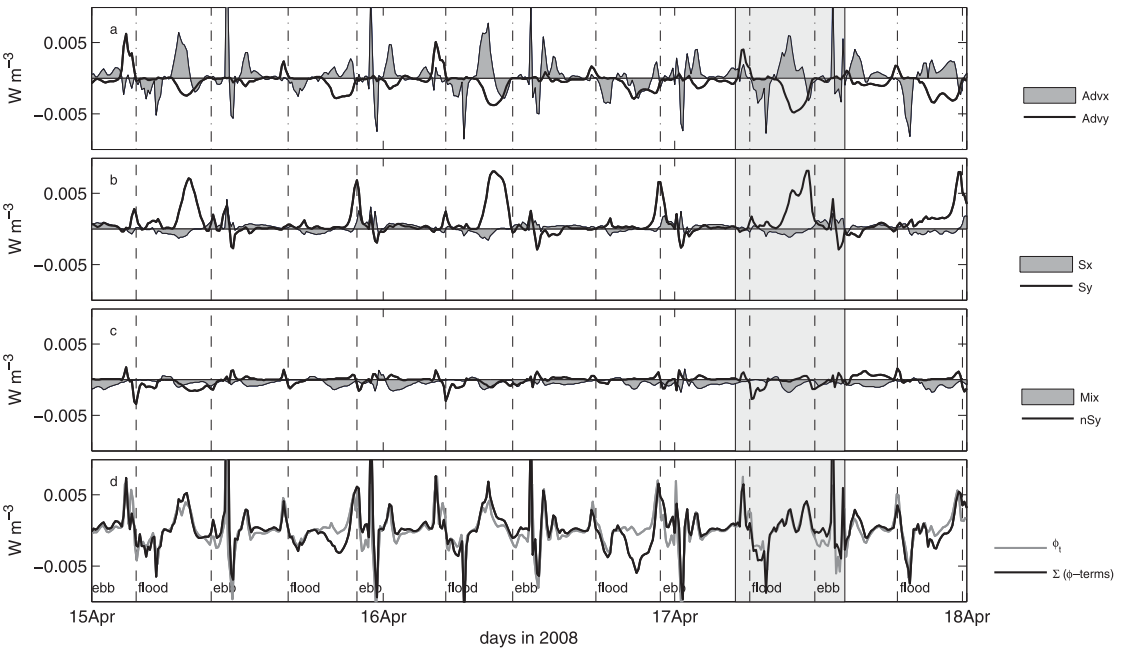

Figure 13. Balance for potential energy anomaly according to equation (3) at station S_2. (a) Along-channel and across-channel advection, **Advx** and **Advy**; (b) along-channel and across-channel straining, **Sx** and **Sy**; (c) vertical mixing, **Mix**, and nonmean across-channel straining, **nSy**; (d) comparison between tendency term and right-hand side of (3), ϕ_t and $\Sigma(\phi$-terms). The gray-shaded area shows the observational period on 17 April at station S_2.

of the calculations (see Figures 12d and 13d). Since both curves agree well, it can be assumed that the calculations are sufficiently accurate.

During the first tidal cycle at full flood on 17 April at S_1 (Figure 12), advection of ϕ (**Advx** and **Advy**) is relatively small. In addition, the depth-mean along-channel straining **Sx** and depth-mean cross-channel straining **Sy** are balancing each other. Nonmean cross-channel straining is small (**nSx** is not shown because it is negligible) and mixing changes between positive (unstable stratification) and negative (stable stratification) contributions just to keep the potential energy anomaly at about neutral level. The overall sum of the forcing terms is thus relatively small at S_1 (see Figure 12d), not leading to significant stratification (see above), except for times of slack tides.

In contrast to that, the sum of the forcing terms is increasing during the course of every other flood tide at station S_2 (first flood tides on 15–17 April; see Figure 13), due to the increasing dominance of depth-mean cross-channel straining. During those flood tides, along-channel and cross-channel advection are partially balancing each other, nonmean cross-channel straining is almost zero and mixing is small, such that strong stratification develops during flood at this station (see also the observations in Figure 5). An explanation for this is the diurnal inequality of the tide which results in a weaker first flood tide and a stronger second flood tide during these days around neap flood (see Figure 3). The weaker flood current results in reduced vertical mixing and thus earlier (already during flood) stratification due to cross-channel density gradients are generated. Since the difference in vertical mixing is not visible in Figure 13c it must be assumed that the major difference in mixing happens further upstream.

It is thus concluded from the transect results for density (see section 5.1) and the analysis of the dynamics of the potential energy anomaly (this section) that an increasing cross-channel density gradient during flood (which is supported by asymmetric freshwater runoff inside the bay) provides available potential energy for generating stratification. This energy is released in the deepest part of the channel, because there the vertically integrated cross-channel density gradient is largest. It is hypothesized that this strong cross-channel density gradient is generated by advection of laterally stratified water from the shallow and wide ebb tidal delta into the deep and narrow Lister Dyb tidal channel where it is funneled due to horizontally convergent flow (as seen in Figure 7a). This has the effect that the cross-channel density gradient is increased until the potential energy is released through a cross-channel exchange current which suddenly increases stratification in the center of the tidal channel (see Figures 4, 5, and 8). It will be attempted in

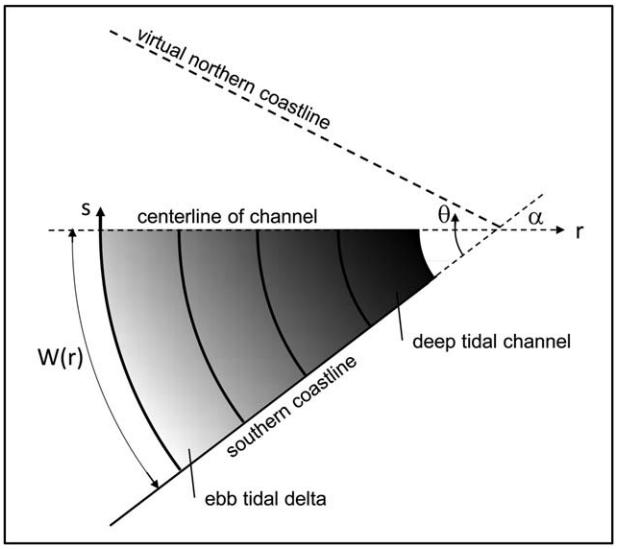

Figure 14. Sketch of the domain and coordinate system for the simple analytical tidal channel in polar coordinates. The gray shading indicates the domain of interest and the water depth increasing from the ebb tidal delta toward the narrow deep channel.

section 6 to confirm this mechanism by examining a simple linear model for buoyancy advection in a horizontally converging channel with constant cross-sectional area.

5.3. Sensitivity to Freshwater Source Location

Additional numerical experiments (not shown) demonstrate the substantial role of the location of freshwater sources within the Sylt-Rømø Bight for the dynamics in the Lister Dyb. When shutting off the river runoff from the two rivers (see Figure 1) and distributing the same amount of freshwater over the entire surface within the Sylt-Rømø Bight, the lateral buoyancy gradient in the Lister Dyb is reduced in such a way that stable flood stratification at S_2 does not occur. The same happens when moving the runoff from the northern river (Brede Å) to the central river (Vidå). It seems that preconditioning of lateral stratification within the Sylt-Rømø Bight is essential for the dynamics in the inlet.

6. Theory

In analogy to tidally averaged conditions where the tendency of the water column to stratify or destratify is characterized by the Simpson number (1), one may also define instantaneous along-channel and cross-channel Simpson numbers

$$\mathrm{Si}_x^i = \frac{\overline{\partial_x b} H^2}{u_*^2}, \qquad \mathrm{Si}_y^i = \frac{\overline{\partial_y b} H^2}{u_*^2}, \tag{4}$$

respectively, with instantaneous values of horizontal buoyancy gradients, water depth, and bottom friction velocity to indicate whether the water column instantaneously has a tendency to stratify or destratify. In contrast to the Simpson number, Si where values of the order of unity indicate transition between tidally averaged mixed and stratified conditions, the instantaneous Simpson numbers Si_x^i and Si_y^i may be interpreted as measures for the acceleration of exchange currents.

To explain the observed sudden occurrence of stable stratification during flood in the center of the tidal channel, we consider a simple analytical model reflecting the conditions for the transition between the wide and shallow ebb tidal delta in the west and the narrow and deep tidal channel east of the tidal delta. The southern half of a wedge-shaped tidal channel is represented with polar coordinates (r, θ) with $r = 0$ at the pole of the coordinate system and $\theta = 0$ at the center of the channel (gray area in Figure 14, with $-r_{\max} \le r \le -r_{\min}$, $0 \le \theta \le \alpha$, and the opening angle α). The dimensional coordinate (in m) across the channel along the arc of circle is denoted as $s = W(r)\theta/\alpha$, where $W(r) = -r\alpha$ is the width of the channel. The bathymetry between the ebb tidal delta and the tidal channel is reproduced by a depth distribution resulting in a constant cross-sectional area: $A = W(r)H(r)$ such that $H = -A/(r\alpha)$. The vertically averaged current velocity along the radial axis (along-channel velocity), $\bar{u}$, is assumed to be constant in time and space and the velocity along the angular coordinate (cross-channel velocity) is zero. Under these conditions, the continuity equation is fulfilled for a constant and zero sea surface elevation. Distribution of vertically averaged buoyancy at slack tide after ebb is approximated by a constant radial buoyancy gradient along the centerline of the channel $\partial_r \bar{b} = \bar{b}_r^0 \ge 0$ ($\theta = 0$) and a constant angular buoyancy gradient $\partial_s \bar{b} = \bar{b}_s^0 \ge 0$ everywhere (see Figure 9 and the discussion in section 5.3):

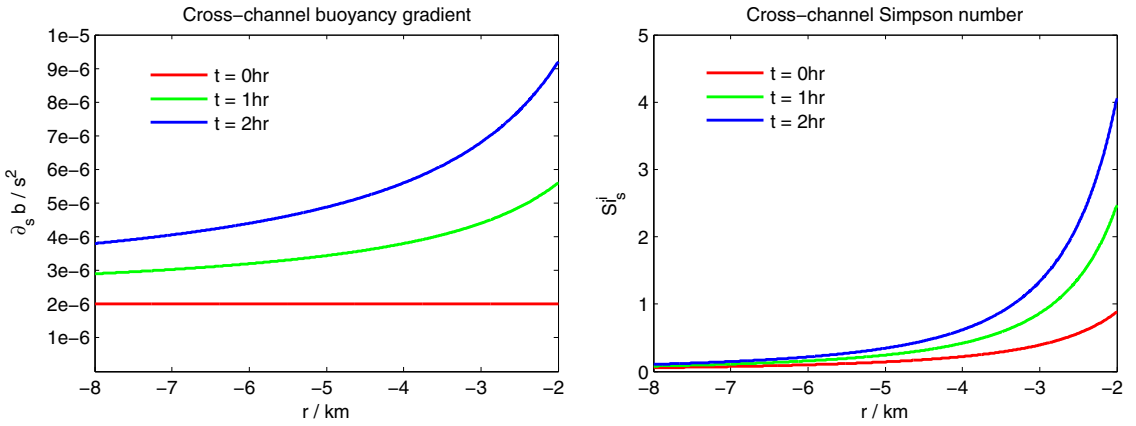

Figure 15. Results from the analytical tidal channel model showing initial conditions (red), conditions after 1 h (green), and conditions after 2 h (blue) as function of the radial coordinate. (left) Cross-channel buoyancy gradient. (right) Cross-channel instantaneous Simpson number.

$$\bar{b}^0(r,\theta)=r\bar{b}_r^0+s\bar{b}_s^0, \tag{5}$$

such that

$$\partial_r\bar{b}^0=\bar{b}_r^0-\theta\bar{b}_s^0. \tag{6}$$

The budget equation for the buoyancy in polar coordinates reads as

$$\partial_t b=-\frac{1}{r}\partial_r(r\bar{u}b)-\partial_z(bw)+\partial_z(K_v\partial_z b), \tag{7}$$

with the vertical velocity w and the eddy diffusivity K_v. Applying kinematic boundary conditions and no-flux conditions at the bottom and the surface and inserting the relation for H, the budget equation for the depth-averaged buoyancy $\bar{b}$ may be written as

$$\partial_t\bar{b}=-\bar{u}\partial_r\bar{b}, \tag{8}$$

meaning that buoyancy changes are proportional to the current velocity and the along-current buoyancy gradient, with the analytical solution

$$\bar{b}=\bar{b}^0-\bar{u}\left(\bar{b}_r^0-\theta\bar{b}_s^0\right)t. \tag{9}$$

With $\theta=s\alpha/W$ and $\partial_s\bar{b}^0=\bar{b}_s^0$ the cross-channel buoyancy gradient increases with time as

$$\partial_s\bar{b}=\bar{b}_s^0\left(1+\bar{u}\alpha\frac{t}{W}\right), \tag{10}$$

with the increase being reciprocal to the width of the channel. In contrast to that, the along-channel buoyancy gradient $\partial_r\bar{b}$ remains constant. Assuming a constant bottom drag coefficient with $u_*^2=c_d\bar{u}^2$, the instantaneous cross-channel Simpson number evolves as

$$\mathrm{Si}_s^i=\frac{\bar{b}_s^0A^2}{c_d\bar{u}^2}\left(\frac{1}{W^2}+\bar{u}\alpha\frac{t}{W^3}\right). \tag{11}$$

Inserting physical quantities roughly estimated from the observations in the Lister Dyb such as $A=2\times10^4$ m^2, $\alpha=30^\circ$, $\bar{u}=1$ m s^{-1}, $\bar{b}_s^0=2\times10^{-6}$ s^{-2} and a typical value for the bottom roughness parameter, $z_0=1\times10^{-3}$m, the conditions shown in Figure 15 for the interval -8 km $\leq r \leq -2$ km are obtained. Both the cross-channel buoyancy gradient and the instantaneous cross-channel Simpson number increase linearly with time, with the highest rate in the deep channel at $r=-2$ km. However, the rate of increase is much higher for the Simpson number, leading after 2 h to values larger than 4 (given the numbers above), values which are indicative for generation of strong exchange flows and generation of stratification. It is

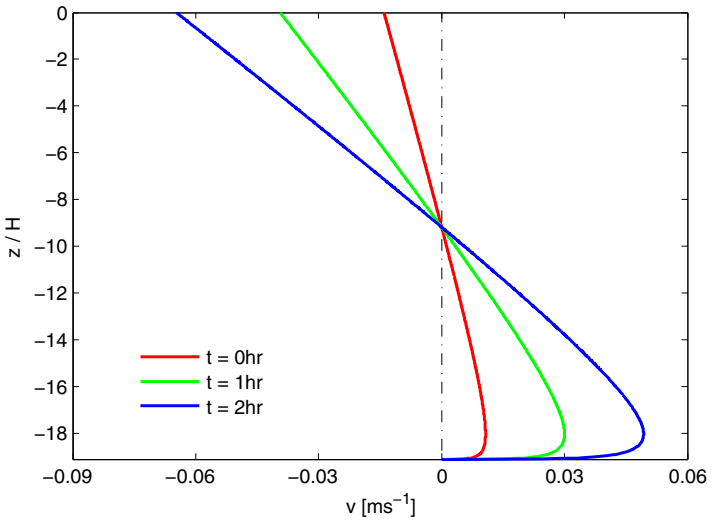

Figure 16. Analytical solution for lateral exchange velocity profiles v at $r = -2$ km at 0, 1, and 2 h after the onset of the flood current.

also clear that a nonzero value of $\bar{b}_s^0$ is essential, because otherwise this mechanism would not be active. Therefore, some asymmetry of freshwater sources inside the Wadden Sea must be given.

To estimate the strength of lateral exchange flows for the present situation, an analytical solution for gravitationally driven estuarine circulation, derived by *Burchard and Hetland* [2010] (their equations (22) and (23)) is modified to represent lateral (instead of longitudinal) flow. This solution is based on the assumption of a stationary pressure-gradient driven flow with parabolic eddy viscosity profile. The potential lateral circulation is just diagnosed here and is not meant to advect longitudinal momentum, such that the original assumption of a nonzero cross-channel velocity still holds. The results are shown in Figure 16. Given the values above, an exchange flow with about ± 0.05 m s^{-1} is resulting at the narrowest part of the tidal inlet ($r = -2$ km). These values are somewhat lower than those observed (see Figures 4 and 5), a fact which may be explained by the neglect of stratification feedback to eddy viscosity in the analytical model. On the other hand, the exchange flow as calculated from the balance between pressure gradient and friction may be slightly overestimated, since the consideration of the acceleration term would reduce the instantaneous cross-channel flow.

Since the cross sections of real tidal channels are not flat, but have the deepest location somewhere in the center, the effect should be enhanced away from the shoals. In this case there would of course also be the compensating effect of higher flood velocity in the deep part of the channel which may increase the bottom friction velocity or which may decrease the lateral density gradient, but the observations suggest that such compensating effects are not dominant.

7. Conclusions

It has been shown during the last few years that the tidally energetic Wadden Sea is subject to a complex thermohaline dynamics [*Burchard et al*., 2008; *Becherer et al*., 2011; *Duran-Matute et al*., 2014]. The results of the present study confirm this finding by proposing a new mechanism for enhancing first cross-channel stratification, then cross-channel exchange flow and consequently vertical stratification in tidal inlets. Laterally weakly stratified conditions at slack after ebb are intensified by horizontally convergent flood currents moving from the wide and shallow ebb tidal delta to the narrow and deep tidal channel, where flood-tide stratification is triggered at its deeper central parts. It seems that the preconditioning of these low-water lateral density gradients by asymmetric freshwater sources within the Wadden Sea is essential. To be efficient, this mechanism requires relatively small vertical mixing. At the present study site, such low mixing occurs only during neap tide in each second tidal cycle. The work of *Becherer et al*. [2011] investigated the observed conditions at the shallow station S_1 and stated that these conditions were classical in the sense that the dynamics could be explained by along-channel straining only. However, stabilizing cross-channel straining was about as strong as destabilizing along-channel straining, such that a pure along-channel SIPS [*Simpson et al*., 1990] was not present. Because the field work at S_2 happened during the weaker of the two diurnal neap tides, it was possible to observe that the cross-channel straining can be a dominant mechanism that drives stratification at this location. The completely different situation observed at station S_2, with substantial stratification occurring already during flood finally motivated this numerical study which revealed the rich complexity of laterally driven dynamics.

It can be assumed that similar processes are present at most other tidal inlets with ebb tidal deltas. The similarity of conditions between this study and the observational study by *Lacy et al*. [2003] in a tidal channel in San Francisco Bay is striking (see the discussion in section 5 of this study). It depends on the exact geometry and the intensity of the tides, whether or not these inlets will at times show distinct flood stratification. Such flood stratification in turn will have strong impacts on estuarine circulation and net sediment transports in these inlet systems and thus deserves further scientific consideration.

Acknowledgments

The present study has been carried out in the framework of the project ECOWS (Role of Estuarine Circulation for Transport of Suspended Particulate Matter in the Wadden Sea) funded by the German Research Foundation (DFG) as project BU1199/11 and by the German Federal Ministry of Research and Education in the framework of the project PACE (The future of the Wadden Sea sediment fluxes: still keeping pace with sea level rise?, FKZ 03F0634A). The work of Henk M. Schuttelaars has been supported by a visiting scientist grant through IOW. The observational station data on which this study is based are available by request to the corresponding author (hans.burchard@io-warnemuende.de).

References

Andersen, T. J., and M. Pejrup (2001), Suspended sediment transport on a temperate, microtidal mudflat in the Danish Wadden Sea, *Mar. Geol.*, *173*, 69–85.

Andersen, T. J., O. Mikkelsen, A. Møller, and M. Pejrup (2000), Deposition and mixing depths on some European intertidal mudflats based on ^{210}Pb and ^{137}Cs activities, *Cont. Shelf Res.*, *20*, 1569–1591.

Banas, N. S., B. M. Hickey, J. A. Newton, and J. L. Ruesink (2007), Tidal exchange, bivalve grazing, and patterns of primary production in Willapa Bay, Washington, USA, *Mar. Ecol. Prog. Ser.*, *341*, 123–139.

Becherer, J., H. Burchard, G. Flöser, V. Mohrholz, and L. Umlauf (2011), Evidence of tidal straining in well-mixed channel flow from microstructure observations, *Geophys. Res. Lett.*, *38*, L17611, doi:10.1029/2011GL049005.

Beusekom, J. E. E. V., and V. de Jonge (2002), Long-term changes in Wadden Sea nutrient cycles: Importance of organic matter import from the North Sea, *Hydrobiologia*, *475–476*, 185–194.

Buijsman, M. C., and H. Ridderinkhof (2008), Variability of secondary currents in a weakly stratified tidal inlet with low curvature, *Cont. Shelf Res.*, *28*, 1711–1723.

Burchard, H., and H. Baumert (1998), The formation of estuarine turbidity maxima due to density effects in the salt wedge. A hydrodynamic process study, *J. Phys. Oceanogr.*, *28*, 309–321.

Burchard, H., and K. Bolding (2002), GETM—A general estuarine transport model, *Tech. Rep. EUR 20253 EN*, Eur. Comm., Ispra, Italy.

Burchard, H., and R. D. Hetland (2010), Quantifying the contributions of tidal straining and gravitational circulation to residual circulation in periodically stratified tidal estuaries, *J. Phys. Oceanogr.*, *40*, 1243–1262.

Burchard, H., and R. Hofmeister (2008), A dynamic equation for the potential energy anomaly for analysing mixing and stratification in estuaries and coastal seas, *Estuarine Coastal Shelf Sci.*, *77*(3), 679–687.

Burchard, H., and H. M. Schuttelaars (2012), Analysis of tidal straining as driver for estuarine circulation in well-mixed estuaries, *J. Phys. Oceanogr.*, *42*, 261–271.

Burchard, H., K. Bolding, and M. R. Villarreal (2004), Three-dimensional modelling of estuarine turbidity maxima in a tidal estuary, *Ocean Dyn.*, *54*, 250–265.

Burchard, H., G. Flöser, J. V. Staneva, T. H. Badewien, and R. Riethmüller (2008), Impact of density gradients on net sediment transport into the Wadden Sea, *J. Phys. Oceanogr.*, *38*, 566–589.

Burchard, H., R. D. Hetland, E. Schulz, and H. Schuttelaars (2011), Drivers of residual estuarine circulation in tidally energetic estuaries: Straight and irrotational channels with parabolic cross section, *J. Phys. Oceanogr.*, *41*, 548–570.

Burchard, H., H. M. Schuttelaars, and W. R. Geyer (2013), Residual sediment fluxes in weakly-to-periodically stratified estuaries and tidal inlets, *J. Phys. Oceanogr.*, *43*, 1841–1861.

Burchard, H., E. Schulz, and H. M. Schuttelaars (2014), Impact of estuarine convergence on residual circulation in tidally energetic estuaries and inlets, *Geophys. Res. Lett.*, *41*, 913–919, doi:10.1002/2013GL058494.

Chernetsky, A., H. M. Schuttelaars, and S. Talke (2010), The effect of tidal asymmetry and temporal settling lag on sediment trapping in tidal estuaries, *Ocean Dyn.*, *60*, 1219–1241.

De Boer, G. J., J. D. Pietrzak, and J. C. Winterwerp (2008), Using the potential energy anomaly equation to investigate tidal straining and advection of stratification in a region of freshwater influence, *Ocean Modell.*, *22*, 1–11.

Duran-Matute, M., T. Gerkema, G. de Boer, J. Nauw, and U. Gräwe (2014), Residual circulation and fresh-water transport in the Dutch Wadden Sea: A numerical modelling study, *Ocean Sci.*, *10*, 611–632.

Festa, J. F., and D. V. Hansen (1978), Turbidity maxima in partially mixed estuaries—A two-dimensional numerical model, *Estuarine Coastal Mar. Sci.*, *7*, 347–359.

Flöser, G., H. Burchard, and R. Riethmüller (2011), Observational evidence for estuarine circulation in the German Wadden Sea, *Cont. Shelf Res.*, *31*, 1633–1639.

Geyer, W. R. (1993), The importance of suppression of turbulence by stratification on the estuarine turbidity maximum, *Estuaries*, *16*, 113–125.

Hansen, D. V., and M. Rattray (1965), Gravitational circulation in straits and estuaries, *J. Mar. Res.*, *23*, 104–122.

Huijts, K. M. H., H. M. Schuttelaars, H. E. de Swart, and C. T. Friedrichs (2009), Analytical study of the transverse distribution of along-channel and transverse residual flows in tidal estuaries, *Cont. Shelf Res.*, *29*, 89–100.

Ianniello, J. P. (1979), Tidally induced residual currents in estuaries of variable breadth and depth, *J. Phys. Oceanogr.*, *9*, 962–974.

Jay, D. A., and J. D. Musiak (1994), Particle trapping in estuarine tidal flows, *J. Geophys. Res.*, *99*, 445–461.

Kondo, J. (1975), Air-sea bulk transfer coefficients in diabatic conditions, *Boundary Layer Meteorol.*, *9*, 91–112.

Lacy, J. R., M. T. Stacey, J. R. Burau, and S. G. Monismith (2003), Interaction of lateral baroclinic forcing and turbulence in an estuary, *J. Geophys. Res.*, *108*(C3), 3089, doi:10.1029/2002JC2001392.

Lang, G., R. Schubert, M. Markowsky, H.-U. Fanger, I. Grabemann, H. L. Krasemann, L. J. R. Neumann, and R. Riethmüller (1989), Data interpretation and numerical modelling of the mud and suspended sediment experiment 1985, *J. Geophys. Res.*, *94*, 14,381–14,393.

Lerczak, J. A., and W. R. Geyer (2004), Modeling the lateral circulation in straight, stratified estuaries, *J. Phys. Oceanogr.*, *34*, 1410–1428.

Lumborg, U., and M. Pejrup (2005), Modelling of cohesive sediment transport in a tidal lagoon an annual budget, *Mar. Geol.*, *218*, 1–16.

Lumborg, U., and A. Windelin (2003), Hydrography and cohesive sediment modelling: Application to the Rømø Dyb tidal area, *J. Mar. Syst.*, *38*, 287–303.

Monismith, S. G., J. R. Burau, and M. Stacey (1996), Stratification dynamics and gravitational circulation in Northern San Francisco Bay, in *San Francisco Bay: The Ecosystem*, edited by J. T. Hollibaugh, pp. 123–153, Am. Assoc. for the Adv. of Sci., Pac. Div., San Francisco, Calif.

Nunes, R. A., and J. H. Simpson (1985), Axial convergence in a well-mixed estuary, *Estuarine Coastal Shelf Sci.*, *20*, 637–649.

Postma, H. (1961), Transport and accumulation of suspended particulate matter in the Dutch Wadden Sea, *Neth. J. Sea Res.*, *1*, 149–190.

Pritchard, D. W. (1952), Salinity distribution and circulation in the Chesapeake Bay estuarine system, *J. Mar. Res.*, *11*, 106–123.
Pritchard, D. W. (1954), A study of the salt balance in a coastal plain estuary, *J. Mar. Res.*, *13*, 133–144.
Rippeth, T. P., N. Fisher, and J. H. Simpson (2001), The semi-diurnal cycle of turbulent dissipation in the presence of tidal straining, *J. Phys. Oceanogr.*, *31*, 2458–2471.
Sanford, L. P., S. E. Suttles, and J. R. Halica (2001), Reconsidering the physics of the Chesapeake Bay estuarine turbidity maximum, *Estuaries*, *24*, 655–669.
Scully, M. E., and W. R. Geyer (2012), The role of advection, straining, and mixing on the tidal variability of estuarine stratification, *J. Phys. Oceanogr.*, *42*, 855–868.
Scully, M. E., W. R. Geyer, and J. A. Lerczak (2009), The influence of lateral advection on the residual estuarine circulation: A numerical modeling study of the Hudson River estuary, *J. Phys. Oceanogr.*, *39*, 107–124.
Simpson, J. H., and D. Bowers (1981), Models of stratification and frontal movement in shelf seas, *Deep Sea Res., Part A*, *28*, 727–738.
Simpson, J. H., J. Brown, J. Matthews, and A. Graham (1990), Tidal straining, density currents, and stirring in the control of estuarine stratification, *Estuaries*, *13*, 125–132.
Simpson, J. H., H. Burchard, N. R. Fisher, and T. P. Rippeth (2002), The semi-diurnal cycle of dissipation in a ROFI: Model-measurement comparisons, *Cont. Shelf Res.*, *22*, 1615–1628.
Stanev, E. V., J.-O. Wolff, H. Burchard, K. Bolding, and G. Flöser (2003), On the circulation in the East Frisian Wadden Sea: Numerical modelling and data analysis, *Ocean Dyn.*, *53*, 27–51.
Umlauf, L., and H. Burchard (2005), Second-order turbulence models for geophysical boundary layers. A review of recent work, *Cont. Shelf Res.*, *25*, 795–827.